Adaptive High-Power Laser-Based Simultaneous Wireless Information and Power Transfer System With Current-Fed Boost MPPT Converter

Yunshi Wang, Changming Zhao, and Liwei Zhang

***Abstract*—A laser beam is an effective power and data carrier that offers inherent advantages in terms of the simultaneous transfer of wireless information and power, which is widely used in both the Internet of Things and the Internet of Energy. This paper proposes an adaptive high-power and high-efficiency laser-based simultaneous wireless information and power transfer system. This is achieved through the use of adjusted and modulated laser diode systems at the transmitter and multiplexed photovoltaic cells, a coupler, a filter, and a maximum power point tracking (MPPT) converter at the receiver. The interaction between the converter and the communication component is investigated theoretically and experimentally using a current-fed boost MPPT converter with the MPPT algorithm of perturbation and observation. The results indicate a maximum DC output power of 7.3 W at the receiver and a maximum MPPT converter efficiency of 84%. Additionally, at a data rate of 495 kbit/s, with a DC output power of 5.11 W, the bit error ratio is 2.62×10^{-4} for the binary amplitude shift keying modulation format, the MPPT converter efficiency is 88%, and the corresponding loss of communication is about 1% of the total transmitted power.**

***Index Terms*—Simultaneous wireless information and power transfer, maximum power point tracking, current-fed boost converter, converter–communication-component interaction.**

I. Introduction

WIRELESS power transfer (WPT) has been widely studied and applied as an important power transfer method [1]–[5]. With the development of Internet of Things and Internet of Energy, new requirements for the wireless transmission of power and data signals have become apparent [6]. The synchronization or time-division transmission of power and data signals is required instead of the use of conventional methods [7], [8]. Among the various WPT technologies, laser/LED-based and microwave-based WPT are suitable for far-field simultaneous wireless information and power transfer (SWIPT) [9], [10].

Manuscript received April 1, 2021; revised June 6, 2021; accepted June 8, 2021. Date of publication June 14, 2021; date of current version July 2, 2021. *(Corresponding author: Changming Zhao.)*

Yunshi Wang and Changming Zhao are with the School of Optics and Photonics, Beijing Institute of Technology, Beijing 100081, China (e-mail: yunshi_wang_bit@sina.com; zhaochangming@bit.edu.cn).

Liwei Zhang is with the CETC China Academy of Electronics and Information Technology, Beijing 100041, China, and also with the Key Laboratory of Photoelectronic Imaging Technology and System, Ministry of Education of China, Beijing, China (e-mail: wyrenzhewudi@126.com).

Digital Object Identifier 10.1109/JPHOT.2021.3088887

Previous studies on LED-based SWIPT were based on optical communication systems incorporating photovoltaic (PV) devices [11]–[13]. However, these studies primarily focused on the transmission of data signals instead of power. Although the system communication bandwidth is considerable, there are no available converters for power control, and discussions on power efficiency are scarce. Furthermore, the transmission power in these studies was often excessively low, making it difficult to realize effective driving capability. A complete high-power SWIPT system should include both a power converter component and a communication component. A high-power laser-based simultaneous wireless information power transfer (LSWIPT) system that is predominantly designed for power transmission should include converters for power control. In a previous study, a boost converter was used at the receiver [14] to realize a laser-based wired simultaneous information and power transfer (SIPT) system with constant voltage output (CVO), using an 808 laser diode (LD) and GaAs PV cells. A 15 W laser was used at the transmitter to obtain a maximum power (MP) of up to 6.2 W at the receiver in the downlink. For a signal transmission rate of 115.2 kbit/s, an additional power loss of 20% was observed. Moreover, another modulated laser was used at the receiver to transmit signals in the uplink.

Unlike laser-based wired SIPT, it is unsuitable to drive the load directly in an LSWIPT system owing to stability and safety issues. LSWPIT systems can be used to charge batteries, which can then provide power to the load. Generally, the receiver of a laser-based WPT system is capable of operating as a solar PV charging system, which can afford at least the maximum power point (MPP) mode and CVO mode based on load demand. However, the system efficiency decreases significantly in the CVO mode than in the MPP mode, regardless of converter efficiency. In this study, we propose a high-power LSWIPT system with a maximum power point tracking (MPPT) converter at the receiver using 808-nm fiber-coupled output LDs and GaAs PV cells. The receiver is capable of continuous operation in the MPP mode during stable operation owing to the use of the MPPT converter and the control of the laser power, which can significantly improve system efficiency. A synchronous rectification current-fed (CF) boost converter with a perturbation and observation (P&O) algorithm is used for MPPT at the receiver. A capacitive coupler is used between the PV cells and the MPPT converter to extract signals from the transmitter

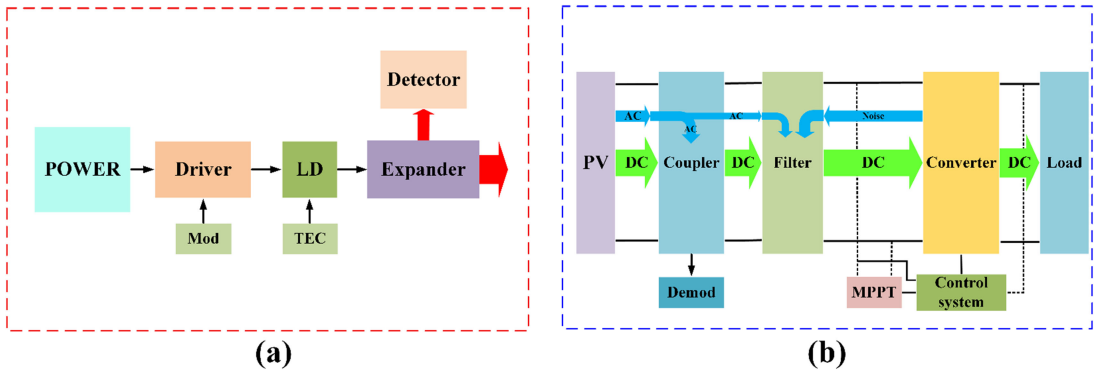

Fig. 1. Proposed LSWIPT system: schematics of the (a) transmitter and (b) receiver.

[15] and reduce the influence of the power disturbance of the modulated laser that is used for communication on the MPPT converter. A signal transformer (0.01–100 MHz) is employed for noise attenuation and electrical isolation. Additionally, a filter is employed between the coupler and MPPT converter for noise attenuation. Further, we discuss the interaction between the power converter and the communication component and conduct a comprehensive analysis and design of the system. And we analyze the system loss. Finally, we achieve a high-efficiency and high-speed LSWIPT system in the MPP mode with a DC power output of up to 7.3 W and limited mutual interference between the transmission of power and data. The power loss associated with the MPPT converter is about 10% of the MP of the PV cells, and the laser power for communication is about 1% of the total transmitted laser power. With a DC power output of 5.2 W, the bit error ratio (BER) is 2.62×10^{-4}, at a data rate of 495 kbit/s, while using the binary amplitude shift keying (2ASK) modulation method with a modulated laser peak-to-peak power of 0.3 W. The transmitted laser power and communication rate can be further increased using optimized devices, with limited interference between the transmitted power and data signals.

The remainder of this paper is organized as follows. Section 2 presents the system structure and working principle; Section 3 discusses the design of the system based on parameters of PV cells and load, and the interaction between the communication and converter components is analyzed. The experimental verification of the system and the experimental analysis of the interaction between communication and signal transmission are presented in Section 4. Lastly, conclusions of this study are highlighted in Section 5.

II. Principle and Model

The proposed LSWIPT system includes both power conversion and communication components. As shown in Fig. 1(a), the proposed system includes a power system, a LD system, modulation devices, and a beam expander at the transmitter. A coupler is essential for signal extraction at the receiver. In high-speed LSWIPT systems, the noise generated by the pulse width modulation (PWM) of the switches overlaps the spectrum of the communication modulation bandwidth, thereby affecting the communication component of the system. Additionally, the PV cells output voltage jitter, caused by the modulated laser, and this also affects the MPPT converter. Therefore, a filter should be employed between the converter and the coupler. As shown in Fig. 1(b), the proposed system includes PV cells, a signal coupler, a filter, a demodulation device, an MPPT converter, a detector for beam waveform monitoring and a constant voltage load at the receiver.

The proposed system functions as follows: the power beam is superimposed on the PV cells for power transmission and communication. Multiplexed PV cells serve as both power and signal conversion devices. The filter inductor suppresses the switching noise, and the coupler obtains the modulated signal and performs demodulation. Additionally, the receiver always operates in the MPP mode according to the power requirements of the constant voltage load through the adjusted laser power at the transmitter and the MPPT converter at the receiver.

As a device that converts both power and data signals, the PV cell model is important in terms of system analyses. For signal extraction analyses, the model of the PV cells can be simplified as shown in Fig. 2(a). This circuit contains a series resistance R_s, shunt resistance R_{sh}, parasitic inductance L_{pv}, parallel capacitance C_{pv} representing the capacitive effect of the p-n junction, and small-signal dynamic resistance R_d representing the diode equivalent effect [13]. In terms of power conversion, the GaAs PV cells operate under a high-power laser, the irradiation of which results in the small size of PV cells. Thus, their capacitance is also considerably much lower than the input capacitance of the CF-boost converter; hence, cell capacitance can be ignored when discussing the effect of PV impedance on converter stability. Thus, the PV model can be simplified as shown in Fig. 2(b); this circuit contains a series resistance R_s, shunt resistance R_{sh}, and small-signal dynamic resistance R_d representing the diode equivalent effect [16]. In terms of analyzing the effect of PV resistance on communication and MPPT converter stability, the PV equivalent impedances at the MPP can be expressed as follows:

$$Z_{pv-\mathrm{com}} = \left(L_{pv}s + R_s + R_{sh} \parallel R_d \parallel (C_{pv}s)^{-1}\right) \quad (1)$$

$$Z_{pv-\mathrm{stab}} = (R_s + R_{sh} \parallel R_d) \quad (2)$$

where $Z_{pv\text{-}com}$ and $Z_{pv\text{-}stab}$ are the PV equivalent impedances of the communication and converter components, respectively. As

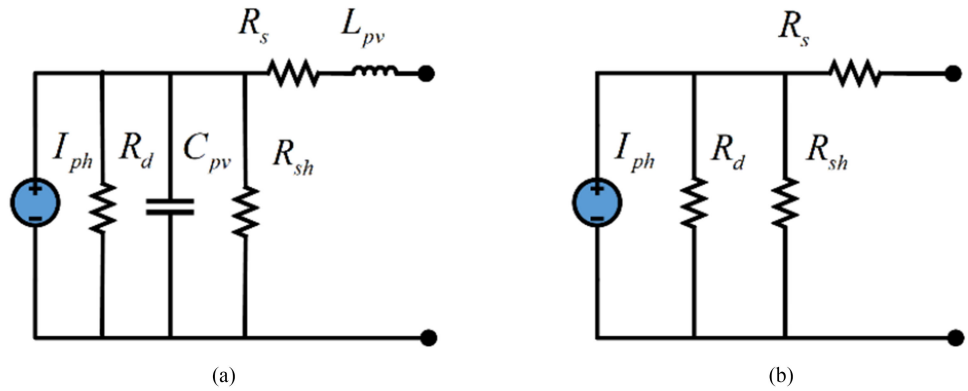

Fig. 2. PV equivalent circuit models for (a) communication and (b) converter stability analysis.

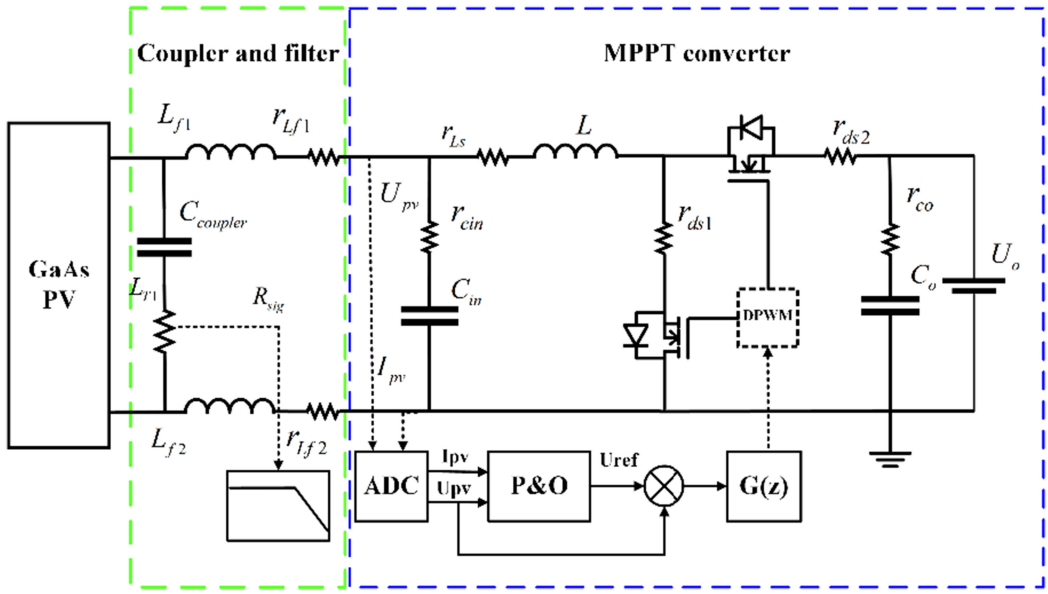

Fig. 3. Circuit diagram of receiver with PV cells, coupler, filter, synchronous rectification CF-boost MPPT converter, and constant voltage load.

PV cells are essentially current sources, input voltage control is applied instead of input current control for the stability and speed of the MPPT converter, as discussed in previous studies [17], [18]. Moreover, a CF converter is used instead of a voltage-fed converter to improve system stability [19], [20]. A synchronous rectification CF-boost converter is used due to its output voltage range and efficiency. The P&O MPPT algorithm, which is easy to implement, is applied in this case [21]. Additionally, a capacitive coupler is used between the PV cells and converter to extract modulation signals from the transmitter. Fig. 3 presents the power stage and control block diagram for the input voltage control CF-boost-based MPPT converter as well as the coupler with a filter for communication. The green dashed part and the blue dashed part in Fig. 3 represent the coupler and filter, and the MPPT converter of the proposed LSWIPT system, respectively.

With an ideal current source, the output voltage of the PV cells, which is approximately equal to the input voltage of the converter in the MPP mode, can be expressed as follows [20], [21]:

$$\hat{u}_{pv} = \frac{Z_{in}}{(1+L_{in})}\hat{i}_{pv} + \frac{T_{oi}}{(1+L_{in})}\hat{u}_o + \frac{L_{in}}{K_s\,(1+L_{in})}\hat{v}_{mpp-ref} \tag{3}$$

where $\hat{\mathrm{u}}_{\mathrm{pv}}$, $\hat{\mathrm{i}}_{\mathrm{pv}}$, $\hat{\mathrm{u}}_{\mathrm{o}}$, and $\hat{\mathrm{d}}$ are small-signal dynamics parameters of the PV output voltage, PV output current, converter output voltage, and converter duty cycle, respectively. Z_{in}, T_{oi}, and G_{ci} are the open-loop input impedance, input and output voltage transfer function, and control input voltage transfer function of the synchronous rectification CF-boost converter, respectively. These variables can be expressed as follows [22]:

$$Z_{in} = \frac{\hat{u}_{in}}{\hat{i}_{in}} = \frac{(sL + r_{\mathrm{L}} + r_{\mathrm{ds}})\,(1 + sr_{\mathrm{Cin}}C_{in})}{LC_{in}s^2 + C_{in}s\,(r_{\mathrm{L}} + r_{\mathrm{ds1}} + r_{\mathrm{Cin}}) + 1} \tag{4}$$

$$T_{oi} = \frac{\hat{u}_{in}}{\hat{u}_o} = \frac{(1-D)\,(1 + sr_{\mathrm{Cin}}C_{in})}{LC_{in}s^2 + C_{in}s\,(r_{\mathrm{L}} + r_{\mathrm{ds}} + r_{\mathrm{Cin}}) + 1} \tag{5}$$

$$G_{ci} = \frac{\hat{u}_{in}}{\hat{d}} = -\frac{(U_{\mathrm{o}} + U_{ds})\,(1 + sr_{\mathrm{Cin}}C_{in})}{L_1C_{in}s^2 + C_{in}s\,(r_{\mathrm{L}} + r_{\mathrm{ds}} + r_{\mathrm{Cin}}) + 1} \tag{6}$$

where $C_{coupler}$, R_{sig}, L_f, r_{Lf}, C_{in}, r_{cin}, L, r_L, D, $C_{\rm o}$, $r_{\rm co}$, and $U_{\rm o}$ are the coupler capacitance, signal sampling resistance, filter inductance, filter inductor resistance, input capacitance, input capacitor equivalent series resistance (ESR), inductance, inductor resistance, duty cycle, output capacitance, output capacitor ESR, and load voltage of the CF-boost MPPT converter, respectively. The upper and lower switch transistor on-resistance and conduction voltage drop of the synchronous rectification CF-boost are r_{ds} and U_{ds}, respectively. L_{in} is the input voltage loop gain of the converter, which can be expressed as follows:

$$L_{in}{=}G_{PI}K_sG_{pwm}G_{ci}\,(s) \tag{7}$$

where K_s is the input voltage sampling coefficient and G_{pwm} is the PWM modulator gain, both of which are constant. G_{PI} is the proportional integral (PI) compensation, which can be expressed as follows:

$$G_{PI}{=}k_P + \frac{k_I}{s} \tag{8}$$

where k_P and k_I are the PI compensation parameters.

The frequency response of the channel formed by $Z_{pv\text{-}com}$, the coupler, the filter, and the converter at the receiver can be expressed as follows:

$$\frac{V\,(\omega)}{I_{ph}\,(\omega)} = \frac{\frac{R_{sig}}{R_{sig}+(C_{sig}s)^{-1}}}{\frac{1}{Z_{pv-com}} + \frac{1}{Z_{sig}} + \frac{1}{Z_{filter}+Z_{in}}} \tag{9}$$

where ω is the angular frequency of the modulated laser. The signal extraction branch impedance Z_{sig} can be expressed as follows:

$$Z_{sig} = R_{sig} + (C_{sig}s)^{-1} \tag{10}$$

Additionally, the filter inductance impedance Z_{filter} can be expressed as follows:

$$Z_{filter} = L_f s + R_{Lf} \tag{11}$$

III. System Design

The external impedance of the MPPT converter is formed by the coupler, filter, and the impedance of the PV cells, which affects the dynamic characteristics of the converter [23], [24]. Additionally, the coupler, filter, and converter also affect the channel. Therefore, a comprehensive design of the communication and converter components in a SWIPT system is required [25]. The primary goal of this system design is to transmit power in a stable and efficient manner. Therefore, the power converter parameters are first determined based on the input and output parameters of the converter, and the communication subsystem is subsequently designed and optimized based on the converter design. Furthermore, the impact of the PV impedance, filter, and coupler on converter stability is discussed along with the impact of the PV impedance, filter, coupler, and converter on the channel.

A. Converter Component

Converter parameters are determined based on the laser power, PV cell output, and load. The peak-to-peak power of the modulated communication laser is significantly smaller than that of the total transmitted laser power. Therefore, its effect on the power conversion of the PV cells is negligible. In the proposed system, the transmitted laser power ranges from 30 to 50 W and the converter output voltage is 5 V. Fig. 4(a–d) present plots of I–V, P–V, I_{ph}–P_{laser} and I_{mpp}–P_{laser}, and (d) P_{mpp}–P_{laser} and F_{mpp}–P_{laser} at a temperature of 35°C. I_{ph} and I_{mpp}, and P_{mpp} and F_{mpp} represent the photocurrent and MPP current, and MP and efficiency of the PV cells for a laser power ranging from 30 to 50 W, respectively.

On neglecting parasitic parameters, the relationships between U_{mpp} and U_o and R_{mpp} and R_L can be expressed, respectively, as follows:

$$(1 - D_{mpp})\,U_o{=}U_{mpp} \tag{12}$$

$$(1 - D_{mpp})^2 R_o{=}R_{mpp} \tag{13}$$

Here, U_o and R_o are the voltage and resistance of the converter, respectively, and D_{mpp} is the duty cycle of the PWM signal at the MPP.

The ripple rate of the converter includes the inductance current ripple rate γ_{IL}, input capacitance voltage ripple rate $\gamma_{\rm Cin}$, and output capacitance voltage ripple rate γ_{Co}. To reduce this ripple noise, the converter needs to operate in the continuous conduction mode. At the MPP, γ_{IL}, $\gamma_{\rm Cin}$, and $\gamma_{\rm Co}$ can be expressed, respectively, as follows [26]:

$$\gamma_{IL} = \frac{U_{mp}\cdot D_{mp}}{L\cdot I_{mp}\cdot f} \tag{14}$$

$$\gamma_{Cin} = \frac{I_{mp}\cdot \gamma_{IL}}{8\cdot U_{mp}\cdot C_{in}\cdot f} \tag{15}$$

$$\gamma_{Co} = \frac{D_{mp}}{R_o\cdot C_o\cdot f} \tag{16}$$

where f, L, C_{in}, and C_o are the switching frequency, inductance, input capacitance, and output capacitance of the MPPT converter, respectively. After a comprehensive consideration of the efficiency and volume, f is set to 200 kHz, and γ_{IL}, γ_{Cin}, and γ_{Co} are set to 30%, 0.1%, and 0.3%, respectively. Furthermore, the values of L, C_{in}, and C_o are 15 μH, 110 μF, and 264 μF, respectively.

B. Communication Component

For high-power LSWIPT systems designed predominantly for power transmission, the size of the PV cell is typically considerably larger than that of a high-speed photodetector; furthermore, its parasitic parameters are not optimized, and to obtain as much power as possible, the PV cell works under a forward bias voltage (FBV). Moreover, the modulated LDs are not specifically designed and packaged for high-speed modulation; this also limits the communication rate of the system. Therefore, the high-power LSWPIT system in the present study performs narrowband communication. Evidently, optimized devices can be used to increase the communication rate when required [27]. The parasitic capacitance of the PV cells is predominantly affected by the bias voltage and temperature [28], [29]. In the

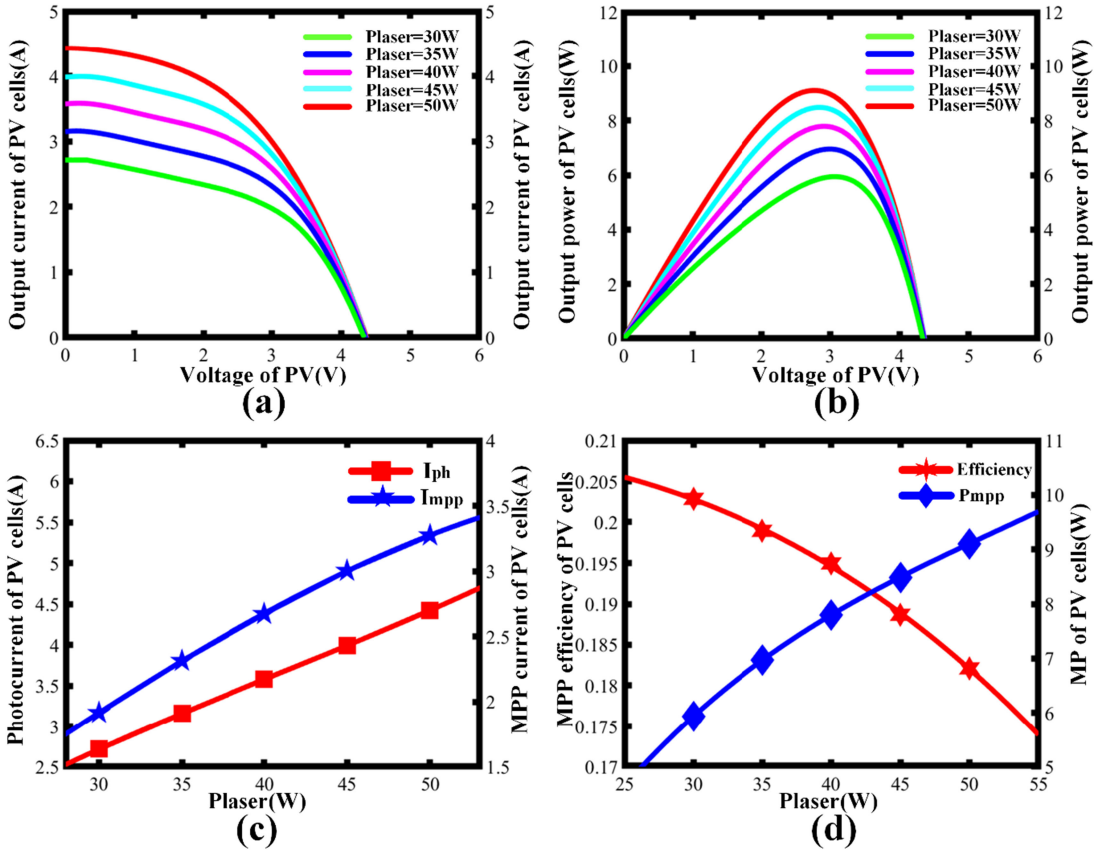

Fig. 4. Plots of (a) I–V, (b) P–V, (c) I_{ph}–P_{laser} and I_{mpp}–P_{laser}, (d) P_{mpp}–P_{laser} and F_{mpp}–P_{laser} for the PV cell for a laser power of 30–50 W.

experiment, a thermo-electric cooler was used to maintain the PV cell at 35°C. The parasitic inductance of the PV cells is nearly unchanged [13].

Filter inductance can meet noise attenuation requirements through attenuation of the fundamental switching frequency noise. The relationship between the fundamental frequency noise of the converter and the corner frequency f_0 of the *LC* filter formed by C_{in} and L_{filter} can be described as follows [30]:

$$f_0 = \sqrt{A} \cdot f_{SMP} \tag{17}$$

where A is the attenuation ratio required for the fundamental frequency noise of the converter, f_{SMP} is the switching frequency, and f_0 is the *LC* filter corner frequency, which can be expressed as follows:

$$f_0 = \frac{1}{2\pi\sqrt{L_{filter} \cdot C_{in}}} \tag{18}$$

The output voltage ripple of the photovoltaic cell is excessively small; hence, the ripple loss of sampling resistance can be ignored.

C. Interaction

The minimum loop gain of a converter with a non-ideal source needs to satisfy the Nyquist or Routh–Hurwitz stability criterion [21], [31]. Stability can be analyzed using the bode plots of Z_{in}, T_{oi}, and G_{ci}. Accounting for the effect of the external impedance of the converter, the output voltage of the PV cells, which is equal to the converter input voltage in the MPP mode, can be expressed as follows [21]:

$$\begin{aligned}\hat{u}_{pv} = & \frac{Z_{o-LCR}Z_{in}}{(Z_{o-LCR}+Z_{in})(1+L_{in})}\hat{i}_{pv} \\ & + \frac{Z_{o-LCR}T_{oi}}{(Z_{o-LCR}+Z_{in})(1+L_{in})}\hat{u}_o \\ & + \frac{Z_{o-LCR}G_{ci}L_{in}^{lcr}}{K_s(Z_{o-LCR}+Z_{in})(1+L_{in}^{lcr})}\hat{v}_{mpp-ref}\end{aligned} \tag{19}$$

where $Z_{o\text{-}LCR}$ is the impedance formed by the PV cells, filter, and coupler; it can be expressed as follows:

$$Z_{o-LCR} = \frac{\begin{pmatrix} L_f C_f (r_{pv}+r_{cf}) s^2 + L_f s + C_f r_{cf} r_{pv} s \\ + C_f r_{Lf} (r_{pv}+r_{cf}) s + r_{pv} + r_{Lf} \end{pmatrix}}{C_f (r_{pv}+r_{cf}) s + 1} \tag{20}$$

Thus, according to Eq. (3) – (6), $Z_{o\text{-}LCR}$ affects the dynamic characteristics of the converter through Z_{in}, T_{oi}, and G_{ci}. As digital control is used in this study, the method described in [32], [33] is employed for approximate analyses of Z_{in}, T_{oi}, and G_{ci} in the discrete domain. The larger the coupling capacitor and the filter inductor, the more significant the impact on the system. Using the obtained parameters, the bode diagrams of Z_{in}, T_{oi}, and G_{ci} of the MPPT converter in the continuous and

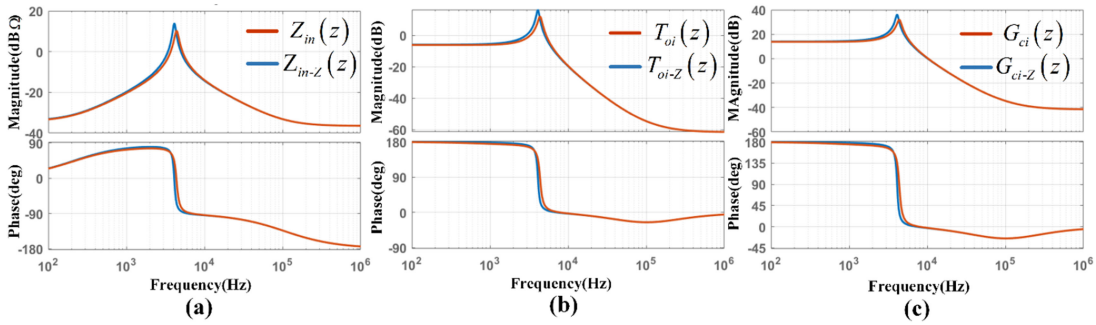

Fig. 5. Bode diagrams of (a) Z_{in}, (b) T_{oi}, and (c) G_{ci} of the CF-Boost MPPT converter in the discrete domain with and without the effect of external impedance $Z_{o\text{-}LCR}$.

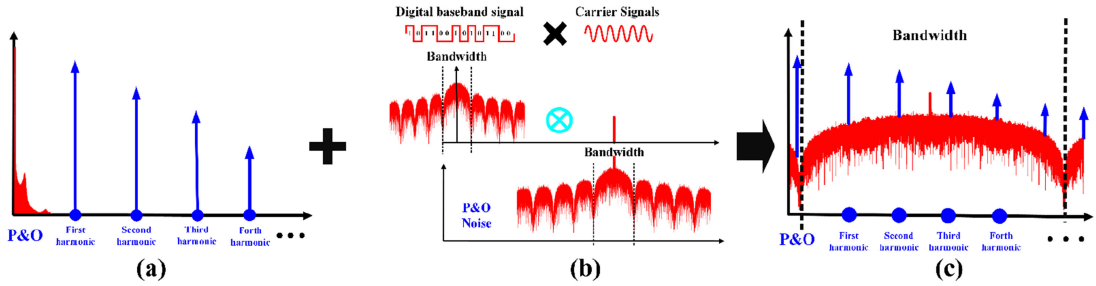

Fig. 6. Spectra of (a) the noise generated by the MPPT converter in the coupler, (b) ideal 2ASK modulation signal generation process, and (c) superposition of the 2ASK modulated signal and the MPPT converter noise from the coupler.

discrete domains could be generated both with and without the incorporation of the effect of $Z_{o\text{-}LCR}$, when the filter inductance was 500 μH and the coupling capacitor was 100 μF, as shown in Figs. 5(a–c), respectively. $Z_{in}(z)$, $T_{oi}(z)$, and $G_{ci}(z)$ represent the corresponding parameters assuming an ideal current source, and $Z_{in\text{-}Z}(z)$, $T_{oi\text{-}Z}(z)$, and $G_{ci\text{-}Z}(z)$ represent the corresponding parameters with $Z_{o\text{-}LCR}$ in the discrete domain. The impact of $Z_{o\text{-}LCR}$ on Z_{in}, T_{oi}, and G_{ci} in the discrete domain is negligible when using the obtained parameters as shown in Fig. 5. Therefore, the proposed system is capable of stable operation as a system with an ideal current source.

In the proposed LSWIPT system, there are two types of MPPT converter noise that affect the channel: the low frequency noise caused by the implementation of P&O and the noise caused by the PWM of the switches. Because of the filter and coupling device, the channel exhibits a bandpass characteristic [13], which is also confirmed through further experiments on the channel amplitude frequency response (CAFR) and the channel phase frequency response (CPFR) below. In addition, within the closed-loop bandwidth of the converter (usually one-fifth to one-tenth of the switching frequency) [30], the low-frequency disturbance of the input laser within the closed-loop bandwidth of the converter has a more significant impact on the steady-state performance of the converter than a higher-frequency disturbance. Digital bandpass modulation is, therefore, employed to adapt to the channel characteristics, negate the overlap of the low frequency P&O noise with the modulation spectrum, reduce the effect of the low frequency noise of the CW laser, and further reduce the impact of the modulated laser low-frequency disturbance on the converter. A simple 2ASK digital bandpass modulation format is adopted for channel evaluation. Complex modulation approaches, such as the improved orthogonal frequency division multiplexing modulation [13] and equalization techniques, can be applied in cases where high communication rates are required when there are no restrictions on the communication power consumption. Fig. 6 presents the relevant spectra of the proposed system.

IV. Experiments

A. Prototype and Specification

As shown in Fig. 7, to verify the proposed system, a high-power (laser power of up to 50 W) LSWIPT system is built using a CF-boost MPPT converter in the MPP mode at a distance of 2m. The LD system at the transmitter is composed of a fiber coupling LD system with a core diameter of 600 μm and a numerical aperture of 0.25. The threshold current and working voltage of the LD system are 1.8 A and 11 V, respectively. After output from an expander with beam splitter, the high-power beam is normally incident approximately coaxial on the four PV cells, which are connected in series with central symmetry. The reflectance of the beam splitter is so high that the transmission power can be ignored compared with the total transmitted power. A detector is used to obtain the waveforms and relative power of the LDs. A control board (STMicroelectronics, STM32F334) is used to apply the converter and the P&O MPPT algorithms [22].

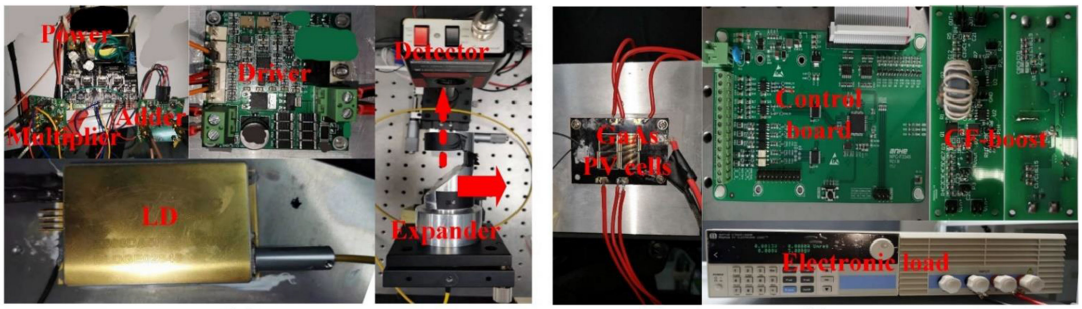

Fig. 7. Photographs of the proposed LSWIPT system prototype: (a) transmitter component and (b) receiver component.

TABLE I
DETAILED SPECIFICATIONS

Component	Parameter	Component	Parameter
Switches ($Q_{1,2}$)	Si2342DS	Resistance of Switches	15 mΩ
Capacitor (C_{in})	110 μF	Capacitor (C_o)	264 μF
Inductance value (L)	15 μH	Inductor Core	55380
Wire resistance of inductor (R_L)	11 mΩ	Filter inductor Core	58548
Filter inductance value ($L_{f1\text{-}2}$, $L_{f2\text{-}2}$)	130 μH	Wire resistance of filter inductor (R_{L2})	30 mΩ
Filter inductance value ($L_{f1\text{-}3}$, $L_{f2\text{-}3}$)	175 μH	Wire resistance of filter inductor (R_{L3})	31 mΩ
Filter inductance value ($L_{f1\text{-}4}$, $L_{f2\text{-}4}$)	219 μH	Wire resistance of filter inductor (R_{L4})	32 mΩ

A constant voltage load (electronic load in the CV mode) of 5 V is employed to simulate the constant voltage characteristics of a lithium battery. A signal transformer (0.01—100 MHz) is employed for noise attenuation and electrical isolation [15]. The 2ASK modulation signal is generated using an arbitrary function generator (Tektronix, AFG3252C), a multiplier (Analog Devices, Inc., AD835), and an adder (Analog Devices, Inc., AD811) at the transmitter. Channel 1 and channel 2 of the arbitrary function generator output a 2^{17}-1 pseudo-random binary sequence and a carrier, respectively. The received signal from the coupler is routed to an oscilloscope (Tektronix, MDO3024) for off-line demodulation. The main parameters of the receiver are presented in Table I.

B. Experimental Results

The proposed high-power LSWIPT system is expected to transfer and convert power in a stable and efficient manner. For this purpose, steady and dynamic experiments were conducted using a MPPT converter with a P&O voltage step of 0.08 V and a perturbation frequency of 10 Hz, both with and without the coupler filter, and 4 W $P_{LD\text{-}2\text{-}P\text{-}P}$ 2ASK modulation with a carrier frequency of 250 kHz and a transmission bit rate of 130 kbit/s. Figs. 8(a–f) present the steady and dynamic waveforms of P_{laser}, $I_{PV\text{-}mpp}$, $U_{PV\text{-}mpp}$, and $I_{o\text{-}MPP}$ in the MPP mode of the proposed system, both with and without the 4 W $P_{LD\text{-}2\text{-}P\text{-}P}$, for laser powers between 50 W and 45 W, 45 W and 40 W, and 40 W and 35 W, respectively. Here, P_{laser}, $I_{o\text{-}MPP}$, and $P_{LD\text{-}2\text{-}P\text{-}P}$ represent the total transmitted laser power, load current, and peak-to-peak power of the modulated laser power, respectively. This can be expressed as $P_{LD\text{-}2\text{-}P\text{-}P} = (P_{LD\text{-}2\text{-}H} - P_{LD\text{-}2\text{-}L})$, where $P_{LD\text{-}2\text{-}H}$ and $P_{LD\text{-}2\text{-}L}$ represent the maximum and minimum peak power of the modulated laser power for communication, respectively. Here, the modulation depth, M_D, is defined as the ratio of $P_{LD\text{-}2\text{-}P\text{-}P}$ to P_{LD1}. The voltage and current of the PV cells fluctuate with $P_{LD\text{-}2\text{-}P\text{-}P}$. However, digital bandpass modulation is adopted for communication, and a low-pass filter with a bandwidth of 5 KHz and a mean filter in the control board are adopted for the voltage and current sampling of the MPPT converter. Therefore, the influence of the voltage and current disturbance of the PV cells on the MPPT controller can be ignored. When the effect of the 438 μH L_{filter} and 80 μF $C_{coupler}$ along with the 4 W $P_{LD\text{-}2\text{-}P\text{-}P}$ 2ASK modulation is considered, it is evident that the system operates suitably in both steady and dynamic states.

The converter parameters have been determined on the basis of the output of the PV cells and the load, as discussed in Section 3. The values of $C_{coupler}$, $P_{LD\text{-}2\text{-}P\text{-}P}$, P_{LD1}, and L_{filter} affect the channel signal-to-noise ratio, and the $C_{coupler}$, P_{LD1}, and L_{filter} also affect the channel characteristics, which have a subsequent impact on the BER of the system. The power of $P_{LD\text{-}2\text{-}P\text{-}P}$ adopted for channel evaluation is 0.2 W, and its effect on the MPPT converter can be ignored. The MPP voltage of the PV cells, which is obtained through P&O, has three voltage values, namely, $U_{mpp\text{-}H}$, $U_{mpp\text{-}M}$, and $U_{mpp\text{-}L}$, which correspond to three channel characteristics. The effects of L_{filter}, $C_{coupler}$, U_{mpp}, and P_{LD1} on the CAFR and CPFR of the system are shown in Figs. 9(a–c), and the corresponding local zooms are shown in Figs. 9(d–h). And the ordinates in Figs. 9(a–h) are relative values. As can be observed, the CAFR of the system presents a bandpass characteristic. With the same L_{filter}, $C_{coupler}$, and P_{LD1}, the CAFR of the system increases as the FBV of the PV cells decreases near the MPP voltage, but the influence of the FBV of the PV cells on the CPFR is so small that it can be ignored in the range of 10 KHz to 1 MHz. The influence of L_{filter} and $C_{coupler}$ on the stability of the converter has been analyzed in Section 3.3. When the value of $C_{coupler}$ is 10, 40, and 80 μF, and L_{filter} is 438, 350, and 260 μH, the system can operate stably, similar to one without $C_{coupler}$ and L_{filter}. When

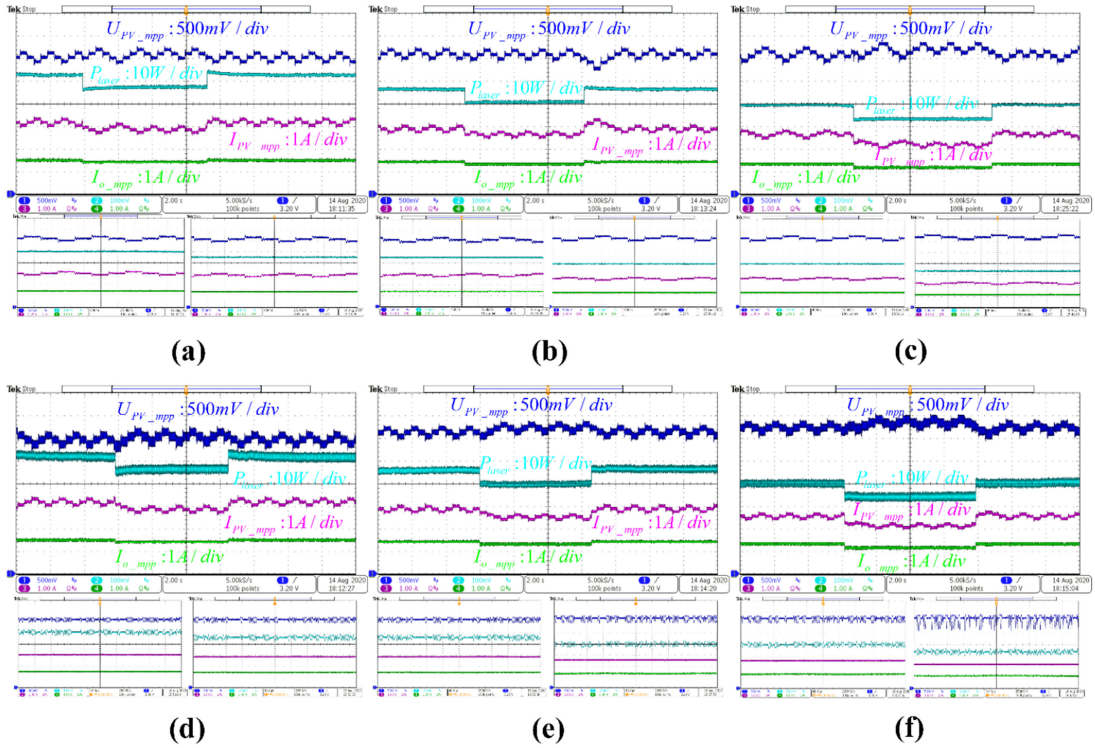

Fig. 8. Steady and dynamic waveforms of P_{laser}, $I_{o\text{-}mpp}$, $U_{PV\text{-}mpp}$, and $I_{PV\text{-}mpp}$ during the MPP mode of wireless power transmission both with and without 4 W $P_{LD\text{-}2\text{-}P\text{-}P}$ 2ASK modulation, for laser powers between (a) and (d) 50 W and 45 W; (b) and (e) 45 W and 40 W; and (c) and (f) 40 W and 35 W.

P_{LD1} is 50 W, the $C_{coupler}$ is 10, 40, and 80 μF, and L_{filter} is 438, 350, and 260 μH. The CAFR and CPFR of the LSWPIT system are shown in Figs. 9(a–b). In the range of 100 Hz to 10 KHz, the CAFR and the CPFR are significantly affected by $C_{coupler}$, whereas they are less affected by L_{filter}. It can be concluded that the larger the $C_{coupler}$ and L_{filter}, the higher the CAFR at a low frequency. In the range of 10 KHz to 1 MHz, the influence of $C_{coupler}$ and L_{filter} on the CAFR and CPFR is not apparent. However, it can still be concluded that the larger $C_{coupler}$ and L_{filter} correspond to a higher CAFR, which is more beneficial for signal transmission in the range of 10 KHz to 1 MHz for digital bandpass signal transmission. Fig. 9(c) presents the CAFR and CPFR when $C_{coupler}$ is 80 μF, L_{filter} is 438 μH, and P_{LD1} is 30, 40, and 50 W. The effect of P_{LD1} on the CPFR is not apparent, whereas the CAFR of the system increases as P_{LD1} decreases, despite the increase in the PV cell voltage, as M_D increases with the decrease in P_{LD1}. Moreover, it can be concluded that the CAFR of the system increases as P_{LD1} decreases, even with the same M_D, as the response of the PV cells near the MPP is positively correlated with its efficiency, which decreases as the laser power increases, with the laser power ranging from 30 to 50 W.

The effect of the small change in CAF near the MPP of the PV cells, which is caused by the change in U_{mmp}, on the BER is so small that it can be ignored. Moreover, the efficiency of the receiving system corresponding to $U_{mpp\text{-}M}$ is the highest among the three values of U_{mpp} obtained using P&O, and only the BER and efficiency associated with $U_{mpp\text{-}M}$ are discussed. The BER, eye diagrams, and corresponding efficiency curves of the receiver with and without the L_{filter}, depending on M_D and P_{LD1}, are compared using 2ASK, with a transmission rate of 495 kbit/s, a carrier frequency of 500 kHz, $C_{coupler}$ of 80 μF, and L_{filter} of 438 μH, as shown in Fig. 10. The eye diagram in Fig. 10 is obtained by demodulating the received 2ASK signal. It is evident that the BER decreases as M_D increases. For the same M_D, the BER decreases with the decrease in P_{LD1}. This is caused by the larger CAFR with a lower power of P_{LD1}. Moreover, according to formula (14–16), the ripple of the CF-boost MPPT converter is proportional to D, and $D = (U_o\text{-}U_{mp})/U_o$. U_o is constant. When the input voltage of the MPPT converter decreases owing to the increase in P_{LD1}, the ripple will become larger, along with the noise and BER.

As shown in Fig. 10, the modulation depth is so low that the impact of the communication subsystem on the power transmission transformation in the dual transmission system is negligible, and the system efficiency decreases with the increase in the modulation depth. The comparison of the receiving system and the MPPT converter with different P_{LD1} and M_D in Fig. 10 indicate that the ESR of the filter inductor will have a small impact on the result of the MPP of the PV cells obtained by the MPPT converter. The impact of the 468 μH L_{filter} and 80 μF $C_{coupler}$ and $P_{LD\text{-}2\text{-}P\text{-}P}$ on the MPP of the PV cells and the system efficiency is considerably small. In the range of 30–50 W, the overall efficiency of the receiving system increases as the laser power decreases. This is because with the decrease in P_{LD1}, the efficiency of the PV cell increases, and the decrease in the PV cell current will lead to a decrease in the filter inductance loss.

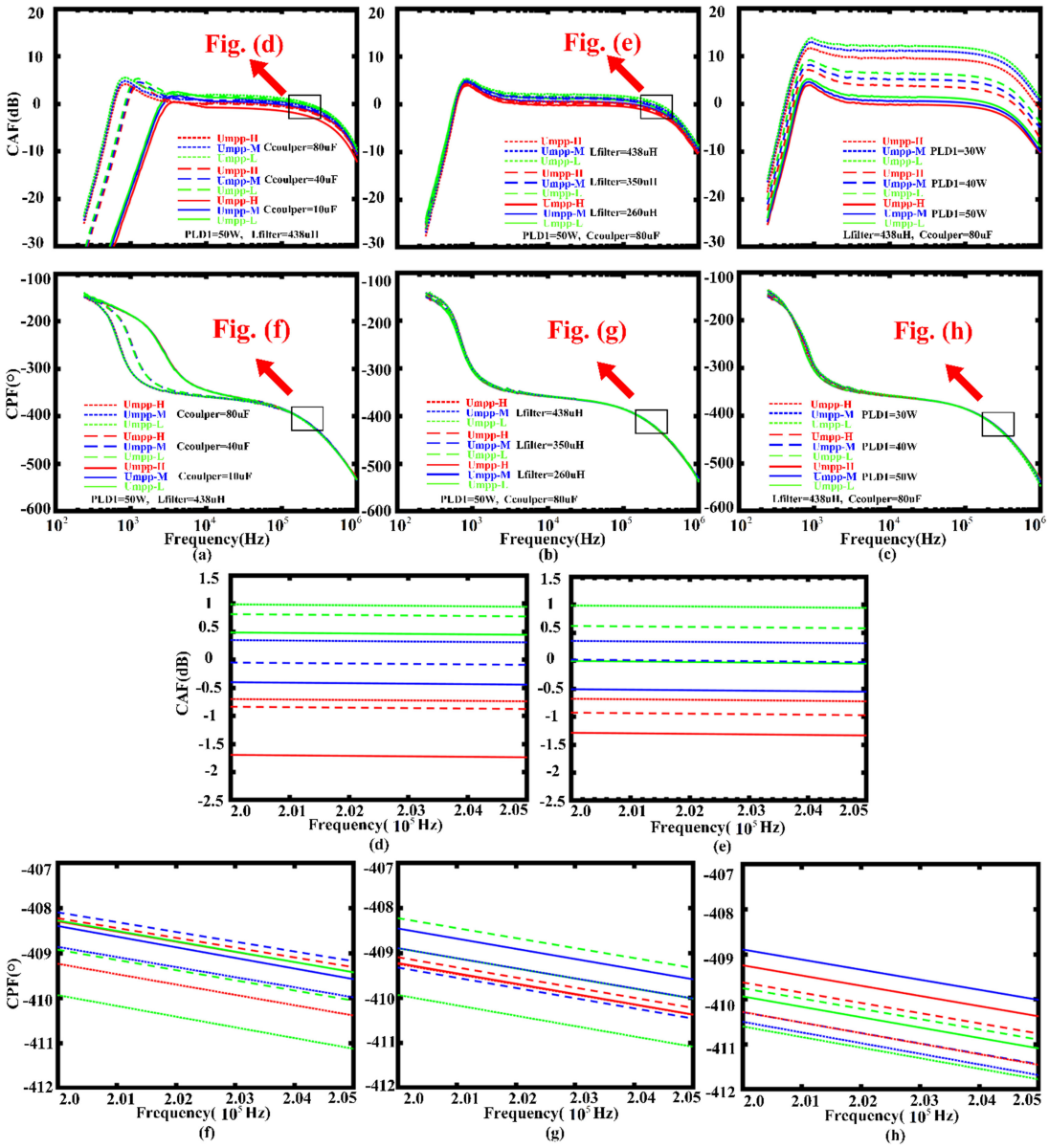

Fig. 9. CAFR and CPFR of the system when (a) P_{LD1} is 50 W, L_{filter} is 438 μH, $C_{coupler}$ is 10 μF, 40 μF, and 80 μF, (b) P_{LD1} is 50 W, $C_{coupler}$ is 80 μF, L_{filter} is 260 μH, 350 μH, and 438 μH, (c) L_{filter} is 438 μH, $C_{coupler}$ is 80 μF, P_{LD1} is 50 W, 40 W, and 30 W; (d) and (e) are the local zooms of CAFR and CPFR in (a), (f) is the local zooms of CPFR in (b), and (g) and (h) are the local zooms of CAFR and CPFR in (c).

C. Loss Distribution

The total loss of the system includes the transmitter loss, transmission loss, and receiver loss. Losses at the transmitter include the losses in the LD driver, LD, and optical system. The losses in the receiver predominantly include the coupler loss, filter inductor loss, and MPPT converter loss. The coupler loss includes the communication loss and converter ripple loss. The power generated by the AC component of the modulated laser can be regarded as the receiver loss. The conduction loss is the main filter inductor loss due to its low current ripple. The MPPT converter loss includes the converter loss and the P&O algorithm loss. The synchronous rectification CF-boost converter loss includes the switching loss, inductor loss, input and output capacitance loss, and conduction loss. The ESR of the input and output capacitance can be reduced using multiple capacitors in parallel. Hence, the capacitance loss can be ignored in the loss analyses. As the input and output current ripple is considerably low, the average current can be used to calculate the sampling resistance loss. The method presented in [36] is applied to analyze the synchronous rectification CF-boost loss. When $C_{coupler}$ is 80 μF, L_{filter} is 438 μH and M_D is 0.1%, the loss distribution in the proposed system for laser power values of 50, 40, and 30 W is presented in Fig. 11. It can be concluded that the main loss of the system is the electro-optical loss in the LD and the photoelectric loss of the PV cell. The loss in the LD driver is also considerable. Therefore, the key to improving the

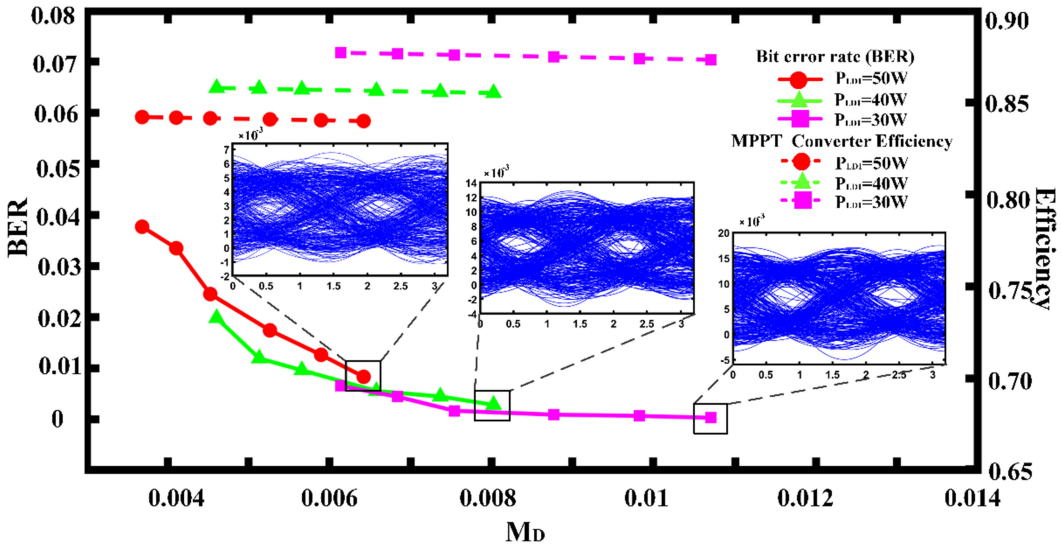

Fig. 10. BER and eye diagram depending on M_D and the corresponding efficiency of the receiving system when L_{filter} is 438 μH, $C_{coupler}$ is 80 μF, and P_{LD1} is 50 W, 40 W, and 30 W, using 2ASK with a constant voltage load of 5 V.

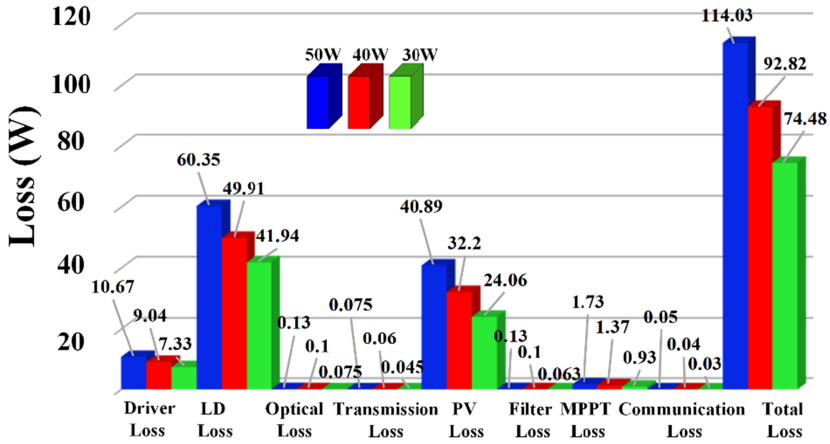

Fig. 11. Loss distribution in the proposed LSWIPT system with $P_{LD\text{-}1} = 50$ W, 40 W, and 30 W and $M_D = 0.1\%$ under a constant voltage load of 5 V.

efficiency of a LSWPIT system is to optimize the efficiency of the laser and PV cells.

V. Conclusion

In this study, a narrowband high-power and high-efficiency LSWIPT system is developed using an adjusted laser power at the transmitter and multiplexed PV cells and an MPPT converter at the receiver. Under the requirement of high-efficiency power transmission, the proposed LSWIPT system, which uses the P&O algorithm and the synchronous rectification CF-boost MPPT converter, is analyzed. The interaction between the converter and communication components is investigated both theoretically and experimentally. The response of the channel and the corresponding bit error rate and efficiency are investigated experimentally. It is shown that the proposed LSWIPT system operates suitably, with limited interaction between the converter and communication components. The maximum output DC power of the receiving system is 7.3 W, with a constant voltage load of 5 V, the bit error ratio is 8.32×10^{-3} using 2ASK modulation format at a data rate of 495 kbit/s. The corresponding loss for communication is about 0.6% of the total transmitted power and the MPPT converter efficiency is 84%. With a DC output power of 5.11 W, the bit error ratio is 2.62×10^{-4} using 2ASK modulation format at a data rate of 495 kbit/s, and the MPPT converter efficiency is 88%, and the corresponding loss for communication is less than 1% of the total transmitted power.

Experiments using a higher power and communication rate can be conducted in the future, with little expected interaction between the transmission of the power and signal. The proposed system is based on an MPPT converter with synchronous rectification CF-boost topology and the P&O algorithm. However, more complex and efficient topologies and MPPT algorithms may also be applicable. Moreover, the GaAs cells and modulated

LD system are not optimized, which limits the efficiency and bandwidth of the entire system. Therefore, in future works, more efficient and higher bandwidth LD systems and GaAs cells and more complex communication modulation formats and equalization technology should be employed for higher efficiency and communication rates [13], [27].

ACKNOWLEDGMENT

The authors wish to thank the anonymous reviewers for their valuable suggestions.

REFERENCES

[1] J. Fakidis, S. Videv, S. Kucera, H. Claussen, and H. Haas, "Indoor optical wireless power transfer to small cells at nighttime," *J. Lightw. Technol.*, vol. 34, pp. 3236–3258, 2016.

[2] H. G. Sandalidis, V. Alexander, T. A. Tsiftsis, and V. Nicholas, "Illumination, data transmission, and energy harvesting: The threefold advantage of VLC," *Appl. Opt.*, vol. 56, no. 12, 2017, Art. no. 3421.

[3] N. Wang *et al.*, "One-to-multipoint laser remote power supply system for wireless sensor networks," *IEEE Sensors J.*, vol. 12, no. 2, pp. 389–396, Feb. 2012.

[4] I. Haydaroglu and S. Mutlu, "Optical power delivery and data transmission in a wireless and batteryless microsystem using a single light emitting diode," *IEEE/ASME J. Microelectromech. Syst.*, vol. 24, no. 1, pp. 155–165, Feb. 2015.

[5] Y. Wang, C. Zhao, L. Zhang, C. Liu, and J. Li, "High-efficiency pulse width modulation-based wireless laser power transmission step-down system," *IEEE Photon. J.*, vol. 12, no. 2, Apr. 2020, Art. no. 8400214.

[6] T. D. P. Perera, D. N. K. Jayakody, S. K. Sharma, S. Chatzinotas, and J. Li, "Simultaneous wireless information and power transfer (SWIPT): Recent advances and future challenges," *IEEE Commun. Surveys Tuts.*, vol. 20, no. 1, pp. 264–302, 2018.

[7] J. Wu, C. Zhao, Z. Lin, J. Du, Y. Hu, and X. He, "Wireless power and data transfer via a common inductive link using frequency division multiplexing," *IEEE Trans. Ind. Electron.*, vol. 62, no. 12, pp. 7810–7820, Dec. 2015.

[8] W. Wang, Q. Zhang, H. Lin, M. Liu, X. Liang, and Q. Liu, "Wireless energy transmission channel modeling in resonant beam charging for IoT devices," *IEEE Internet Things J.*, vol. 6, no. 2, pp. 3976–3986, Apr. 2019.

[9] Y. Liu, H.-Y. Chen, K. Liang, C.-W. Hsu, C.-W. Chow, and C.-H. Yeh, "Visible light communication using receivers of camera image sensor and solar cell," *IEEE Photon. J.*, vol. 8, no. 1, Feb. 2016, Art. no. 7800107.

[10] P. D. Diamantoulakis and G. K. Karagiannidis, "Simultaneous lightwave information and power transfer (SLIPT) for indoor IoT applications," in *Proc. Global Commun. Conf.*, 2017, pp. 1–6.

[11] S.-M. Kim, J.-S. Won, and S.-H. Nahm, "Simultaneous reception of solar power and visible light communication using a solar cell," *Opt. Eng.*, vol. 53, no. 4, 2014, Art. no. 046103.

[12] W. H. Shin, S. H. Yang, D. H. Kwon, and S. K. Han, "Self-reverse-biased solar panel optical receiver for simultaneous visible light communication and energy harvesting," *Opt. Exp.*, vol. 24, no. 22, 2016, Art. no. A1300.

[13] Z. Wang, D. Tsonev, S. Videv, and H. Haas, "On the design of a solar-panel receiver for optical wireless communications with simultaneous energy harvesting," *IEEE J. Sel. Areas Commun.*, vol. 33, no. 8, pp. 1612–1623, Aug. 2015.

[14] H. Helmers, C. Armbruster, M. V. Ravenstein, D. Derix, and C. Schoner, "6-W optical power link with integrated optical data transmission," *IEEE Trans. Power Electron.*, vol. 35, no. 8, pp. 7904–7909, Aug. 2020.

[15] I. B. Valmala, G. Bumiller, H. A. Latchman, M. V. Ribeiro, and L. W. Yonge, *Power Line Communications: Theory and Applications for Narrowband and Broadband Communications over Power Lines*. 2010.

[16] L. Nousiainen *et al.*, "Photovoltaic generator as an input source for power electronic converters," *IEEE Trans. Power Electron.*, vol. 28, no. 6, pp. 3028–3038, 2013.

[17] W. Xiao, W. G. Dunford, P. R. Palmer, and A. Capel, "Regulation of photovoltaic voltage," *IEEE Trans. Ind. Electron.*, vol. 54, no. 3, pp. 1365–1374, 2007.

[18] A. Urtasun, P. Sanchis, and L. Marroyo, "Adaptive voltage control of the DC/DC boost stage in PV converters with small input capacitor," *IEEE Trans. Power Electron.*, vol. 28, no. 11, pp. 5038–5048, Nov. 2013.

[19] T. Suntio, J. Leppaaho, J. Huusari, and L. Nousiainen, "Issues on solar-generator interfacing with current-fed MPP-tracking converters," *IEEE Trans. Power Electron.*, vol. 25, no. 9, pp. 2409–2419, Sep. 2010.

[20] J. Viinamaki, J. Jokipii, T. Messo, T. Suntio, M. Sitbon, and A. Kuperman, "Comprehensive dynamic analysis of photovoltaic generator interfacing DC–DC boost power stage," *IET Renewable Power Gener.*, vol. 9, no. 4, pp. 306–314, 2015.

[21] T. Suntio, T. M., and J. Puukko, *Power Electronic Converters - Dynamics and Control in Conventional and Renewable Energy Applications*. 2017.

[22] [Online]. Available: https://www.stmicroelectronics.com.cn/content/ccc/resource/technical/document/application_note/ec/9c/b0/81/b5/12/4e/21/DM00108726.pdf/files/DM00108726.pdf/jcr:content/translations/en.DM00108726.pdf

[23] T. Suntio, J. Viinamaki, J. Jokipii, T. Messo, and A. Kuperman, "Dynamic characterization of power electronic interfaces," *IEEE J. Emerg. Sel. Topics Power Electron.*, vol. 2, no. 4, pp. 949–961, Dec. 2014.

[24] L. Qin, S. Xie, M. Hu, and C. Yang, "Stable operating area of photovoltaic cells feeding DC-DC converter in output voltage regulation mode," *IET Renew. Power Gener.*, vol. 9, no. 8, pp. 970–981, 2015.

[25] X. He, R. Wang, J. Wu, and W. Li, "Nature of power electronics and integration of power conversion with communication for talkative power," *Nature Commun.*, vol. 11, no. 1, 2020, Art. no. 2479.

[26] R. Ayop and C. W. Tan, "Design of boost converter based on maximum power point resistance for photovoltaic applications," *Sol. Energy*, vol. 160, pp. 322–335, 2018.

[27] J. Fakidis, S. Videv, H. Helmers, and H. Haas, "0.5-Gb/s OFDM-based laser data and power transfer using a GaAS photovoltaic cell," *IEEE Photon. Technol. Lett.*, vol. 30, no. 9. pp. 841–844, May 2018.

[28] K. A. Kim, C. Xu, L. Jin, and P. T. Krein, "A dynamic photovoltaic model incorporating capacitive and reverse-bias characteristics," *IEEE J. Photovolt.*, vol. 3, no. 4, pp. 1334–1341, Apr. 2013.

[29] W. Kim, V. Duong, T. Nguyen, and W. Choi, "Analysis of the effects of inverter ripple current on a photovoltaic power system by using an AC impedance model of the solar cell," *Renew. Energy*, vol. 59, pp. 150–157, 2013.

[30] J. Wang *et al.*, "A novel method for the determination of dynamic resistance for photovoltaic modules," *Energy*, vol. 36, no. 10, pp. 5968–5974, 2011.

[31] C. Basso, *Switch-Mode Power Supplies Spice Simulations and Practical Designs*. New York, NY, USA: McGraw-Hill, 2008.

[32] B. Choi, *Pulsewidth Modulated DC-to-DC Power Conversion: Circuits, Dynamics, and Control Designs*. Piscataway, NJ, USA: IEEE Press, 2013.

[33] L. Corradini *et al.*, *Digital Control of High-Frequency Switched-Mode Power Converters*. Hoboken, NJ, USA: Wiley, 2015.

[34] Z. Guo, Y. Zhu, and D. Sha, "Zero-voltage-switching asymmetrical PWM full-bridge DC-DC converter with reduced circulating current," *IEEE Trans. Ind. Electron.*, vol. 68, no. 5, pp. 3840–3853, May 2021.